S-Duct with Boundary Layer Ingestion: Geometry Optimization and Validation

Catherine Clark[1], Faezeh Rasimarzabadi[2],
Hamza abo el Ella[3], and Hugo Breton[4]
National Research Council Canada, Ottawa, Ontario, K1A 0R6, Canada

Inès Chikhaoui[5] and David W. Zingg[6]
University of Toronto, Toronto, Ontario, M3H 5T6, Canada

The National Research Council Canada Aerospace Research Centre is collaborating with the University of Toronto Institute for Aerospace Studies to develop an experimentally-validated numerical optimization tool that produces a propulsor intake geometry optimized to minimize circumferential flow distortion and pressure losses. The goal is to eventually apply this tool to the design of future low-emission aircraft concepts that incorporate S-ducts with boundary layer ingestion. The first phase of testing, which did not include a fan, was completed in the NRC's Gas Turbine Lab Test Cell 1. After the empty test rig pressure calibrations and boundary layer generator calibrations, the main test program was completed by measuring the pressure distribution over the S-duct inlet and outlet areas, as well as various locations within the interior of the S-duct. The measurements were completed at inlet speeds of Mach 0.16 and Mach 0.19, and inlet boundary layer thicknesses varying from 20% to 69%. The experimental data shows good agreement with the CFD predictions, confirming the ability of the optimization algorithm to produce an optimized S-duct geometry with low circumferential flow distortion. The results include a discussion on the sensitivity of the S-duct performance to inlet boundary layer thickness and Mach number.

Nomenclature

A	=	area
D	=	jet diameter
P_S	=	static pressure
P_T	=	total pressure
R	=	ratio of the jet to free-stream mass flow rate
V	=	velocity
x	=	streamwise position
y	=	spanwise position
z	=	vertical position
α	=	flow angle
ρ	=	air density
θ	=	angular position/direction

[1] Senior Research Officer, Aerodynamics Laboratory, AIAA Member
[2] Associate Research Officer, Gas Turbine Laboratory
[3] Senior Research Officer, Gas Turbine Laboratory
[4] Senior Mechanical Designer, Design and Fabrication Services
[5] PhD Candidate, Institute for Aerospace Studies
[6] Professor, Institute for Aerospace Studies

I. Introduction

In a conventional aircraft configuration, engines are typically mounted under the wing or above the fuselage such that they are ingesting free stream air far away from the aircraft fuselage. One strategy to improve aircraft efficiency is to place the engines in such a way that they are ingesting a portion of the aircraft fuselage boundary layer; aptly called a boundary layer ingestion (BLI) configuration [1-3]. BLI works by ingesting the airframe boundary layer and accelerating it to provide thrust, leading to a reduction of the aircraft drag [4-6]. This is typically achieved by placing the engines just on top of the rear of the aircraft, or by sinking the engines into the back of the aircraft and directing the boundary layer laden air to the engine via a duct. The result is reduced aircraft fuel burn resulting in lower carbon emissions. In practice however, utilizing BLI introduces two major challenges for the engine design: non-uniform flow going to the engine fan, and potentially increased pressure losses due to the required ducting. The work presented in this paper focuses on aerodynamic optimization of the S-duct with the aim of reducing flow non-uniformity and pressure losses.

The National Research Council of Canada (NRC) Aerospace Research Centre (ARC) has been active in boundary-layer ingestion (BLI) propulsion research since 2018, engaging with several collaborative partners from industry and academia. Early collaborative research projects focused on numerical tools for optimizing propulsor intakes for BLI configurations [7][8], followed by a project with industry focusing on experimental testing of a BLI-tolerant tail-mounted fan [9][10].

The current research project, titled Boundary Layer Ingestion Propulsion Modelling and oPtimization (BLI-ProMaP), is a collaboration between the NRC Low-Emissions Aviation Program and the University of Toronto Institute for Aerospace Studies (UTIAS). The ultimate objective of the project is to produce an experimentally-validated numerical optimization tool that provides a propulsor intake geometry and fan stage geometry for a given BLI cruise flight condition and thrust specification. This work is being completed in coordination with the European Union Investigation and Maturation of Technologies for Hybrid Electric Propulsion (IMOTHEP) program. The NRC and UTIAS are official partners of IMOTHEP.

To achieve the project objective, a staged approach is being taken over a period of three years in order to allow both NRC and UTIAS to build confidence and expertise as the optimization tool and experimental rig are developed. During the first phase of the project, presented in this paper, UTIAS optimized a model-scale S-duct geometry that was based on an IMOTHEP blended wing body concept intake geometry. The NRC designed, built and commissioned a boundary layer control system and test rig in a sub-scale engine test cell to experimentally validate the S-duct simulations. For the second phase of the project, UTIAS will further develop their optimization tool to include fan effects, and the NRC will validate the updated tool with a representative scaled fan installed in the test rig. For the third phase of the project UTIAS will include a fan blade geometry optimization tool in their software and the resulting geometry will be tested by the NRC. The final, validated tool is expected to be of great value in the development of future, low-emission aircraft concepts.

II. UTIAS Aerodynamic Shape Optimization Methodology

The methodology used for the aerodynamic shape optimization software can be broken down into five main components: geometry parameterization and control, mesh deformation, flow evaluation, gradient computation, and the optimization algorithm. A gradient-based formulation is used to minimize a composite objective function that combines flow distortion and pressure losses.

To parameterize the geometry and enable grid deformation, the grid is fitted to a B-spline control volume using spatially-varying knot vectors [11]. The B-spline control points on the duct surface are embedded inside a free-form deformation (FFD) lattice. These lattice points become the design variables that drive the deformation of the embedded surface [12]. The optimization algorithm updates the design variable vector, which determines the shape of the duct as the design progresses towards optimality. A major advantage of the current approach using B-spline patches to parametrize the geometry is that, in contrast to other popular approaches where surface grid nodes are used to parameterize the geometry, an analytical representation of the geometry is maintained throughout the optimization. The flow solver is a parallel, implicit, multi-block structured finite-difference solver that is used to solve the three-dimensional Reynold-averaged Navier-Stokes equations, fully coupled with the Spalart-Allmaras one-equation turbulence model [13]. The computational domain is discretized into a multi-block structured, O-topology grid. The adjoint method is implemented based on extensive hand linearization, as described by Osusky et al. [14]. The overall methodology has been carefully cross-validated with a distinct methodology, demonstrating consistent results for complex aircraft optimization problems [15]. Application of the methodology to optimize an S-duct to minimize combinations of distortion, pressure losses, and swirl at transonic speed are reported in Chiang et al. [16], where it was demonstrated that substantial reductions in circumferential flow distortion are possible through numerical optimization.

The inlet shape, S-duct length, offset, diffusion ratio and exit diameter are fixed during the optimization, while the cross-sectional shape along the S-duct length is allowed to vary within the limits prescribed by the NRC test rig geometry (±10% of the baseline cross-sectional diameters). The following composite objective function is minimized by the optimization algorithm, with the subscript 0 denoting the baseline values used to normalize each objective:

$$J = 0.2\frac{\mathrm{PR}_0}{\mathrm{PR}} + 0.8\frac{DI}{DI_0} \tag{1}$$

The total pressure recovery (PR) and distortion (DI) are defined as follows, where the outlet is partitioned into 'm' rings with 'n' radial elements in each ring.

$$PR = \frac{P_{t,outlet}}{P_{t,inlet}} \tag{2}$$

$$DI = \sum_j^m \left(\sum_i^n \frac{\left(P_{t,i} - P_{t,avg,j}\right)^2 dA_i}{A_j} \right) \tag{3}$$

An additional parameter, swirl (S), is used separately from the objective function to help evaluate the outlet profile characteristics, and is defined as:

$$S\ [rad] = \frac{1}{A_{total}} \sum_j^m \sum_i^n |\alpha_i|\ dA_i \tag{4}$$

The flow angularity (α) is defined as:

$$\alpha[\mathrm{rad}] = \arctan\left(\frac{V_\theta}{V_x}\right) \tag{5}$$

For this first phase of this research program, the geometry optimization is performed at a target total inlet pressure of 64 kPa, a freestream inlet Mach number of 0.16, and a boundary layer thickness of 35% of the inlet height. Total pressure is specified at the upstream boundary, while the downstream static pressure is determined to achieve the desired mean Mach number at the inlet outside the incoming boundary layer. The S-duct length-to-offset ratio is fixed at 2.88 and the diffusion ratio is fixed at 1.3373, based on a concept IMOTHEP geometry presented in spring 2022 in a meeting between IMOTHEP, UTIAS and NRC. The outlet is maintained as a fixed circular geometry capable of containing a rotor with an 18 cm tip diameter. The baseline duct was taken as a simple blend between the rectangular inlet and circular outlet, with no particular attention paid to the geometry along the length of the duct. The multiblock structured grid used for the flow evaluation during the optimization has 1.25 million nodes; experiments with finer meshes showed negligible changes in quantities of interest. Geometry control is accomplished through fourteen 8×8 FFD cross sections. Experiments in Chiang et al. [16] show this provides sufficiently fine geometry control, without enabling excessive control such that the optimized geometry is difficult to manufacture and optimization convergence is compromised.

The optimization converged deeply in 72 iterations such that the gradient is reduced by roughly two orders of magnitude and further changes in the objective function are negligible. For the initial geometry, the PR is 0.9958 and the DI is 3.8×10^{-4}. For the optimized geometry, the PR is 0.9974 and the DI is 3.1×10^{-5}; hence the optimization reduces the circumferential flow distortion by over an order of magnitude while simultaneously reducing pressure losses. Different trades between reductions in pressure losses and distortion are possible by varying the composite objective function, as shown by Chiang et al. [16]. The focus of this project is not to examine these trades, but rather to validate the ability of the optimizer to reduce circumferential distortion.

The cross-sectional changes between the baseline and the optimized duct are shown on the left of Fig. 1, and the final optimized duct is shown on the right of Fig. 1. The second and third sections on the left highlight the formation of one channel at the top and three channels at the bottom, as well as the dips on each side generated by the shape optimization. The more downstream cross-sections show less variations between the baseline and the optimized duct due to the geometric constraint imposed at the outlet. A comparison between the baseline and optimized duct geometry total pressure profiles at the outlet is shown in Fig. 2.

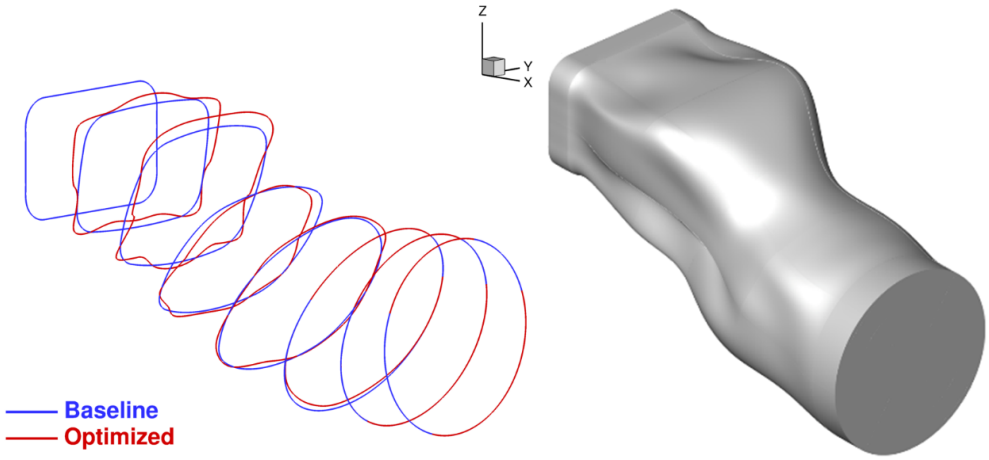

Fig. 1 Baseline vs. Optimized Geometries

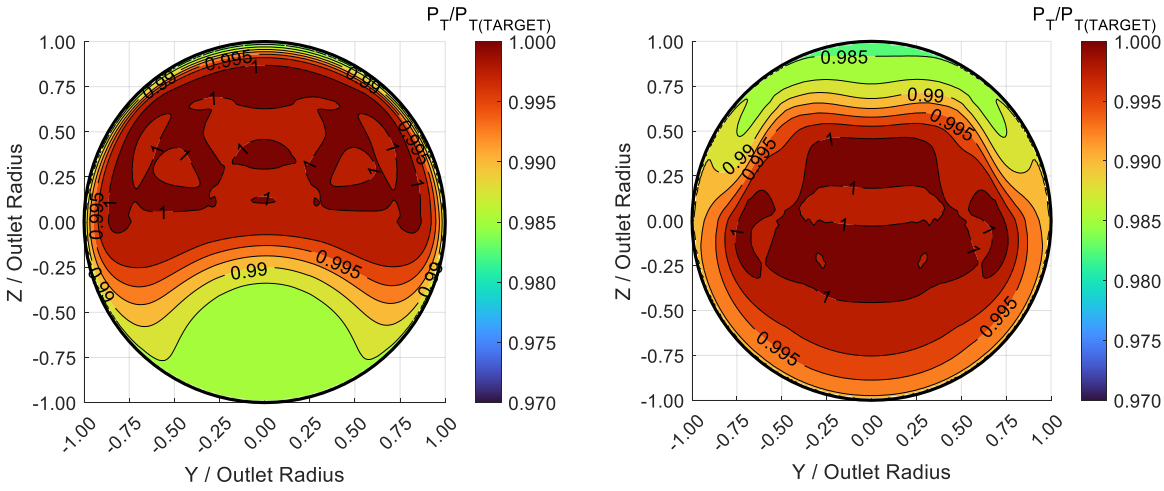

a) Baseline Duct
PR = 0.9958, DI = 3.8×10^{-4}

b) Optimized Duct
PR = 0.9974, DI = 3.1×10^{-5}

Fig. 2 Baseline vs. Optimized Outlet Total Pressure Profiles

III. Facility Description

The test rig used to validate the performance of the optimized S-duct geometry was developed for the NRC Test Cell 1 in building M-7 at the NRC Montreal Road Campus in Ottawa, Ontario, Canada. Although not used for this phase of the research program, the design includes accommodation for a fan and electric motor downstream of the S-duct outlet for testing planned in mid-2024. A schematic of the test rig with the main components identified is shown in Fig. 3.

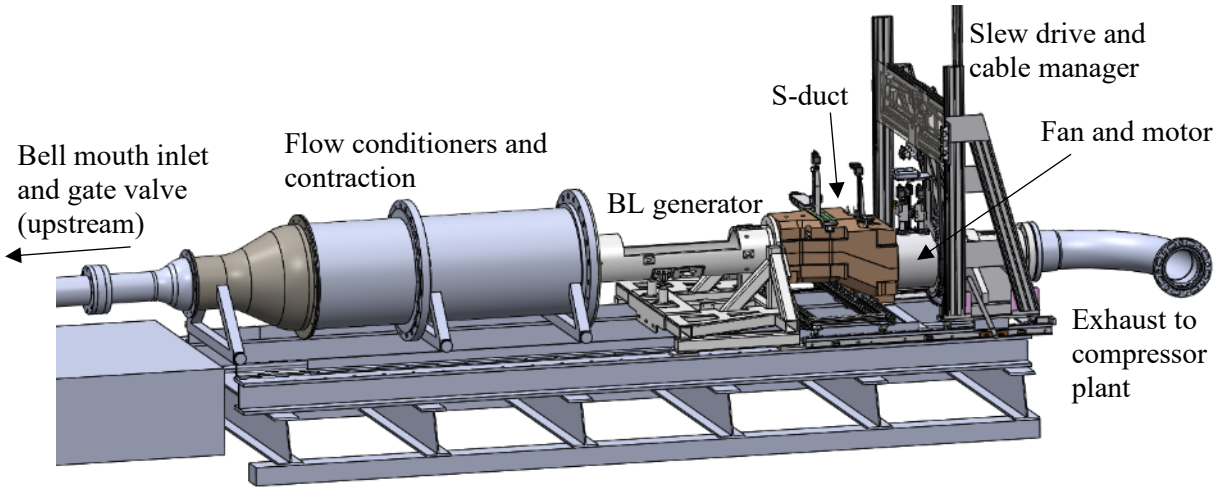

Fig. 3 Test Rig Schematic

A. Bell Mouth Inlet and Gate Valve

The air is drawn into the test rig through a bell mouth located upstream of the test section, with the target air flow supplied using a compressor in a separate building. A gate valve is used to control the pressure in the rig and simulate altitude by lowering the total pressure. As the altitude increases, the air density and therefore mass flow rate through the rig decreases for a given compressor set-point, while the velocity stays approximately constant.

B. Flow Conditioners and Contraction

The flow conditioners consist of a series of perforated plates followed by mesh screens and a contraction. The perforated plates are designed to create a more uniform distribution of the flow over the cross-sectional area downstream of the gate valve, while the pressure loss also increases the simulated altitude in the test section. The flow conditioning meshes are located in the section with the largest cross-sectional area upstream of the test section and are followed by a contraction to further improve the flow uniformity and reduce the turbulence entering the test section. There is a static pressure tap located upstream of the contraction and a ring of four pneumatically-averaged static pressure taps downstream of the contraction to provide a measurement of the static pressure drop through the contraction. This pressure differential is correlated to the total and static pressures at the S-duct inlet during the test rig calibrations.

C. Boundary Layer Generator

The purpose of the boundary layer generator (BLG) is to thicken the boundary layer approaching the S-duct inlet to simulate varying levels of boundary layer thicknesses that develop over a blended wing body aircraft concept. As opposed to previous tests in this facility, which used a radial BLG to simulate ingestion into a tail-mounted engine [10], this simulates a boundary layer approaching the inlet over a large, relatively uniform surface flush with the bottom of the S-duct inlet. The BLG uses high-pressure air blown through a perforated plate to produce a series of jets in cross-flow, as shown in Fig. 4.

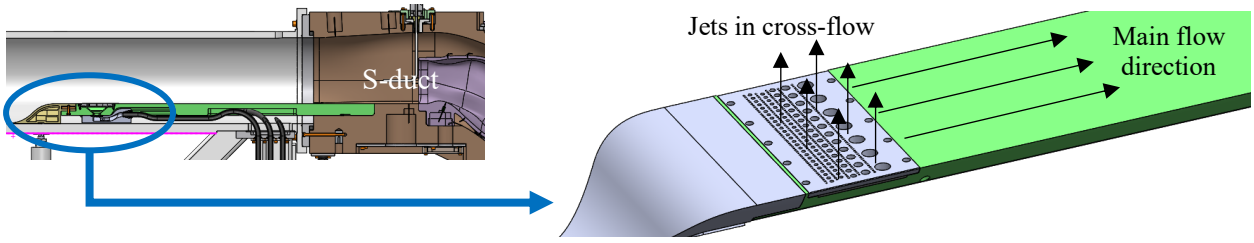

Fig. 4 Boundary Layer Generator Design

The perforated plate design is based mainly on Ref. [17] and Ref. [18]. The plate is designed to not only increase the boundary layer thickness, but also to maintain a natural turbulent boundary layer velocity profile and turbulence intensity levels. The near-wall penetration of a jet into the freestream is approximated using Eq. 6 [19].

$$\frac{z}{RD} = 1.35\left(\frac{x}{RD}\right)^{0.28} \tag{6}$$

where:

- z is the vertical penetration distance from the wall (m)
- x is the streamwise distance from the BLG to the S-duct inlet (m)
- R is the ratio of the jet to free-stream velocity
- D is the jet (hole) diameter (m)

The ratio R is modified for this test in order to account for the change in air density between the BLG and the test rig operating at altitude, such that:

$$R = \frac{\rho_{jet} V_{jet}}{\rho_{\infty} V_{\infty}} \tag{7}$$

where:

- ρ_{jet} is the air density of the BLG jet (kg/m^3)
- V_{jet} is the velocity of the BLG jet (m/s)
- ρ_{∞} is the air density of the main test rig freestream (kg/m^3)
- V_{∞} is the velocity of the main test rig freestream (m/s)

Larger diameter jets penetrate further into the free stream and produce turbulence further away from the wall, so to maintain the desired turbulence distribution in the boundary layer an array of jet diameters is used. Assuming a triangular approximation for the boundary layer turbulence profile, the required jet diameter distributions can be calculated by assuming the area fraction for each hole diameter under the turbulence curve matches the area fraction for the perforated area on the plate. The jet penetration distribution for a triangular turbulence intensity profile is provided in Fig. 5, showing the relative area ratios needed from each hole diameter to maintain a triangular profile. The hole distribution in the machined plate was designed to provide similar area ratios. It should be noted that these calculations assume the jets do not interact with each other. The parameters of the machined BLG plate are provided in Table 1. The ratio of the spacing between holes in the cross-stream direction and the hole diameter is maintained at approximately two, in order to maintain consistent impact of the lateral jet interactions across all jet diameters.

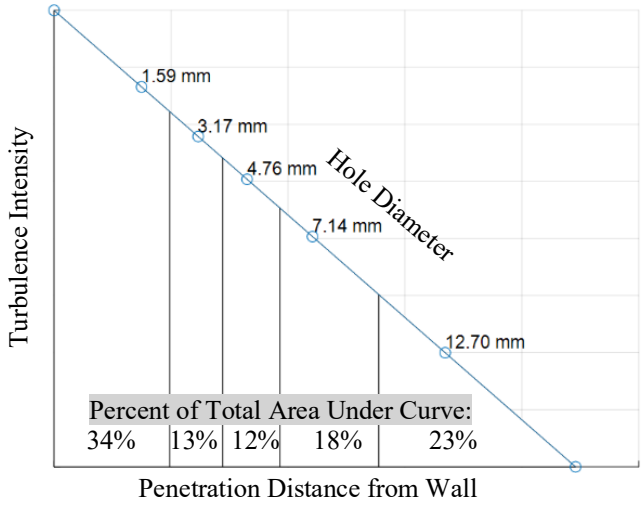

Fig. 5 Jet Penetration vs Turbulence Intensity Target Distribution

Table 1 Perforation Distribution for Boundary Layer Generator Plate

Hole Diameter	Total Number of Holes	Number of Rows	Lateral Pitch/Diameter
1.59 mm (1/16″)	268	5	1.99
3.17 mm (1/8″)	53	2	2.01
4.76 mm (3/16″)	18	1	2.03
7.14 mm (9/32″)	12	1	2.06
12.70 mm (1/2″)	7	1	2.05

D. S-duct and Bypass Design

A schematic of the S-duct installed in the test rig is shown in Fig. 6. At the inlet of the S-duct there is a small, fixed portion that is designed to ensure the S-duct merges smoothly with the floor of the BLG. The outlet of the S-duct terminates in a 10 cm long straight extension prior to the fan location. This extension was added to help the UTIAS computational solution converge once the fan simulation is included. The remainder of the S-duct geometry between the inlet and the outlet is designed based on the UTIAS optimization code. The total length of the S-duct is 335 mm; this was the maximum length possible given the physical constraints of the facility in order to provide the UTIAS code the most flexibility in its optimization algorithm while maintaining the desired geometric ratios. The as-built S-duct was scanned after manufacturing (3D printed ABS-like SLA material), and the maximum deviation between the as-built and the target geometry was approximately 2 mm near the mid-span ceiling, while most other deviations were less than 0.5 mm.

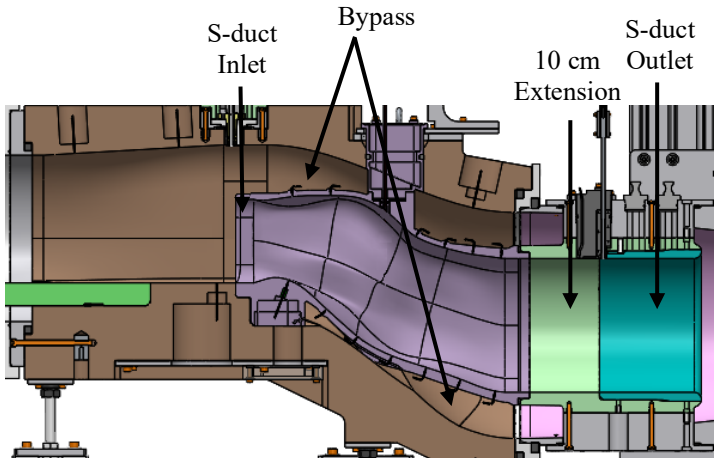

Fig. 6 S-duct and Bypass Design

IV. Facility Calibrations

A. Centerline Total and Static Pressure

The total and static pressure calibration establishes the relationship between the pressure differential through the contraction and the total and static pressures (and therefore velocity and mass flow rate) at the inlet of the S-duct. The calibration was completed with the mass flow through the BLG set to zero and a pitot-static probe was mounted at the centerline of the S-duct inlet. The data were collected at three different gate valve positions.

The maximum achievable velocity at the centerline of the S-duct inlet varies between Mach 0.28 (95 m/s, P_T=45 kPa) with the gate valve fully-open and Mach 0.25 (83 m/s, P_T=38 kPa) with the gate valve half-closed. This is significantly higher than the estimated top speed of Mach 0.16 that the S-duct was optimized for, and is due to modifications to the exit pipe completed prior to the test program that reduced the pressure losses through the circuit. Future phases of testing may consider a higher airspeed for the optimization simulations, to bring the target conditions closer to realistic aircraft operating speeds. There were no observable effects of the gate valve position on the total and static pressure calibrations, indicating the flow distortion introduced by the valve has minimal effect on the test section flow due to the flow conditioning devices between the valve and the test section. Based on the stated accuracies of the instrumentation, the calculated centerline velocity from the calibration has an uncertainty of ±0.51% at the target test condition of 64 kPa total pressure and Mach 0.16.

The turbulence intensity at the inlet was measured at a fixed number of points using a hot-wire probe in the freestream flow outside the boundary layer. At the target operating condition, the average measured turbulence intensity was 1.6% with a standard deviation of ±0.08. The turbulence intensity is not an input parameter for the CFD, and was only measured to help obtain a complete understanding of the flow in the test rig.

B. Boundary Layer Generator

The BLG calibration establishes the relationship between the mass flow rate through the BLG perforated plate, the mass flow rate through the test section and the boundary layer thickness at the S-duct inlet. This calibration was completed using a Kiel probe traversed vertically at three spanwise locations (centerline and ±30% span) immediately upstream of the S-duct inlet, with refinement of the traverser spacing near the floor. It is assumed that the BLG is sufficiently far downstream from the P_{S_UP} pressure taps that when the BLG is activated it does not impact the previously established centerline calibration, which is used to calculate the test section mass flow rate. The BLG calibration results are presented in Fig. 7 based on the mean boundary layer thickness, where the error bars are based on the maximum and minimum boundary layer thicknesses measured across the three spanwise positions. Also plotted in Fig. 7 are the expected boundary layer thicknesses based on the theory used to design the perforated plate.

The results show that the boundary layer thickness as a function of the ratio of the BLG mass flow to the test rig mass flow is relatively insensitive to freestream velocity and there is an increase in spanwise non-uniformity as the BLG mass flow rate increases. Adjustments to the BLG flow path under the plate are planned for future tests in an effort to improve the spanwise uniformity at the higher BLG flow rates. The experiment and theory match at the lowest mass flow rates, but the experimental boundary layer thicknesses increase up to 30% higher than theory at the higher mass flow rates. This is likely due to some of the assumptions made with the theoretical predictions (no interaction between jets, uniform velocity distribution between all jets) versus the reality of the experiment. The linear trend line fitted through the data is used to calculate the boundary layer thickness entering the S-duct inlet during the main test program.

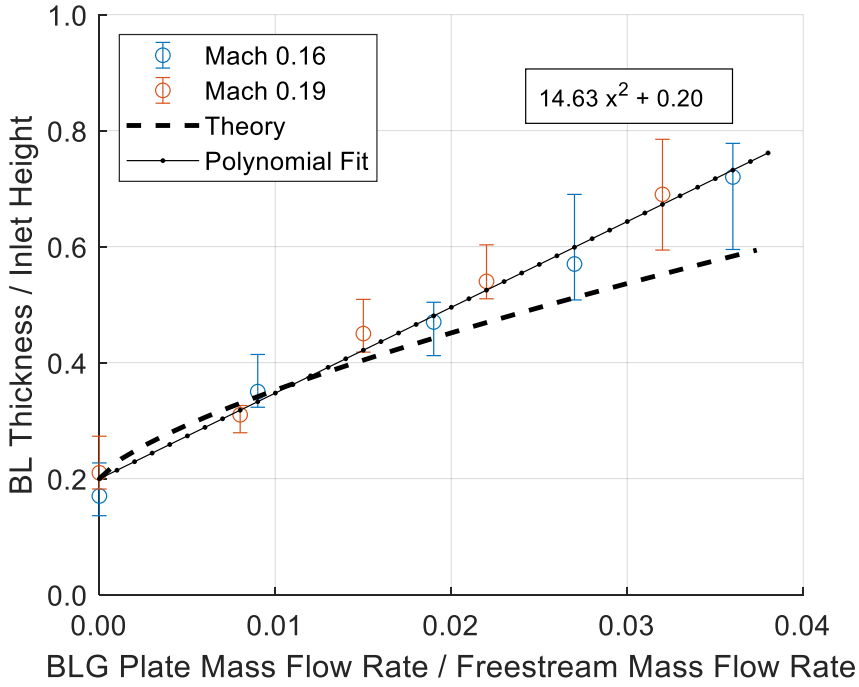

Fig. 7 Boundary Layer Generator Calibration Results

V. UTIAS Optimized Geometry Validation

The UTIAS optimization was performed at a target total pressure of 64 kPa, a freestream inlet Mach number of 0.16, and a boundary layer thickness of 35% of the inlet height. As previously mentioned, the goal of the experimental test program is to validate the UTIAS optimizer CFD predictions of the S-duct performance at these conditions.

A. Inlet Profiles

The first step in the validation of the CFD results was to ensure that the inlet conditions to the CFD domain matched the experimental inlet conditions. A comparison of the CFD and experimental inlet Mach contours is provided in Fig. 8 and the centerline total pressure and Mach number profiles are provided in Fig. 9.

In order to ensure that no significant flow field features were missed due to the coarseness of the traverse grid in the experiment, a run was completed at the target condition with a refined grid. The results do not show any significant differences between the two. The refined grid took approximately twice as long to run as the coarse grid.

The CFD simulations set the total pressure profile at the inlet boundary, and allow the static pressure (and therefore Mach number) to vary according to the simulation calculations. The CFD and experimental total pressure profiles match very well at the inlet, with the exception of a small spike in the CFD total pressure profile just below the ceiling of the duct, which appears to be non-physical. The CFD and experimental Mach contours are similar as well, indicating a small overshoot above the target Mach number just below centerline, a decrease in Mach number towards the upper surface of the duct and a decrease in Mach number near the side walls. There is also a small spike in the Mach number just below the ceiling of the duct with the CFD, corresponding to the spike in total pressure at the same location. Overall, the CFD predicts a slightly higher Mach number outside of the floor boundary layer than the experimental data. One potential source of the differences between the CFD and experiment is the scope of the domains; the CFD simulation domain only includes the interior of the S-duct, while the experimental set-up has a bypass section that can impact the pressure distribution.

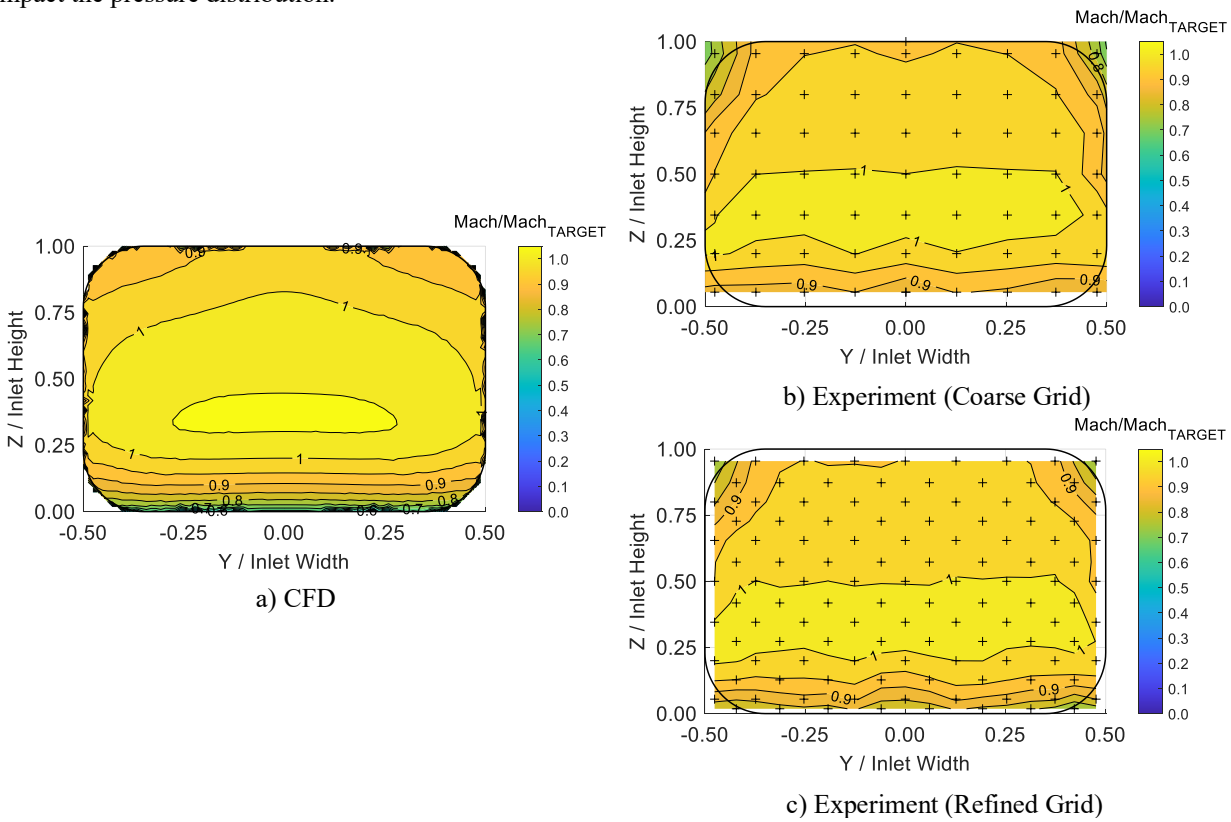

Fig. 8 Target Condition Inlet Mach Contours

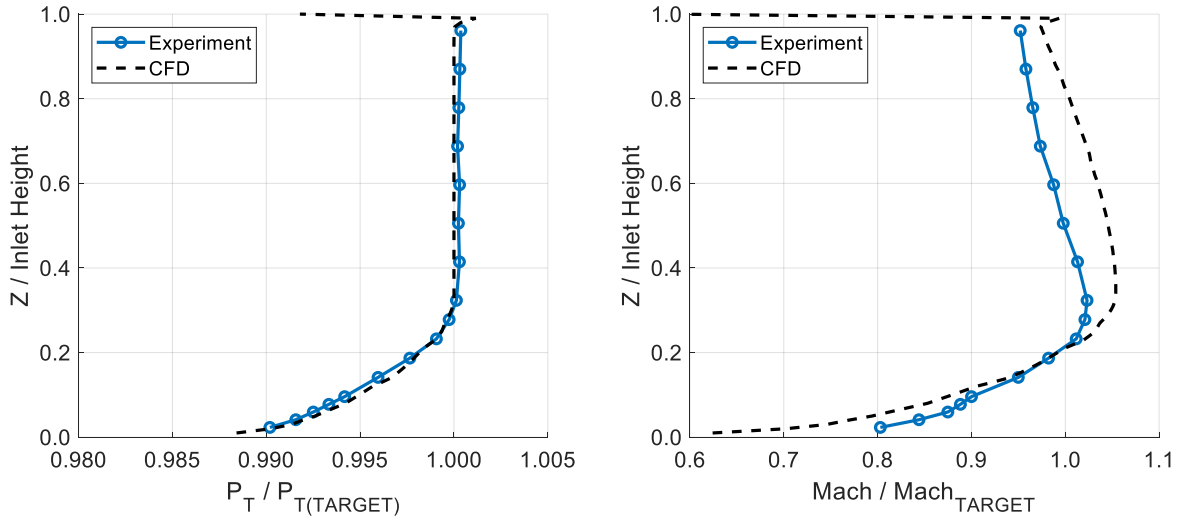

Fig. 9 Target Condition Inlet Centerline Profiles

B. Flow Within Duct

The traverse system located at the mid-length point of S-duct (approximately 190 mm downstream from the leading edge) allows for measurement of the total pressure vertically within the duct. The total pressure profiles measured experimentally in the duct are compared to the CFD in Fig. 10. The results show good agreement between the CFD and experimental total pressure profiles in the lower half of the duct. In the upper half of the duct, the experimental ceiling boundary layer thickens more than the CFD towards the outlet and the CFD continues to have a small, non-physical peak in the total pressure.

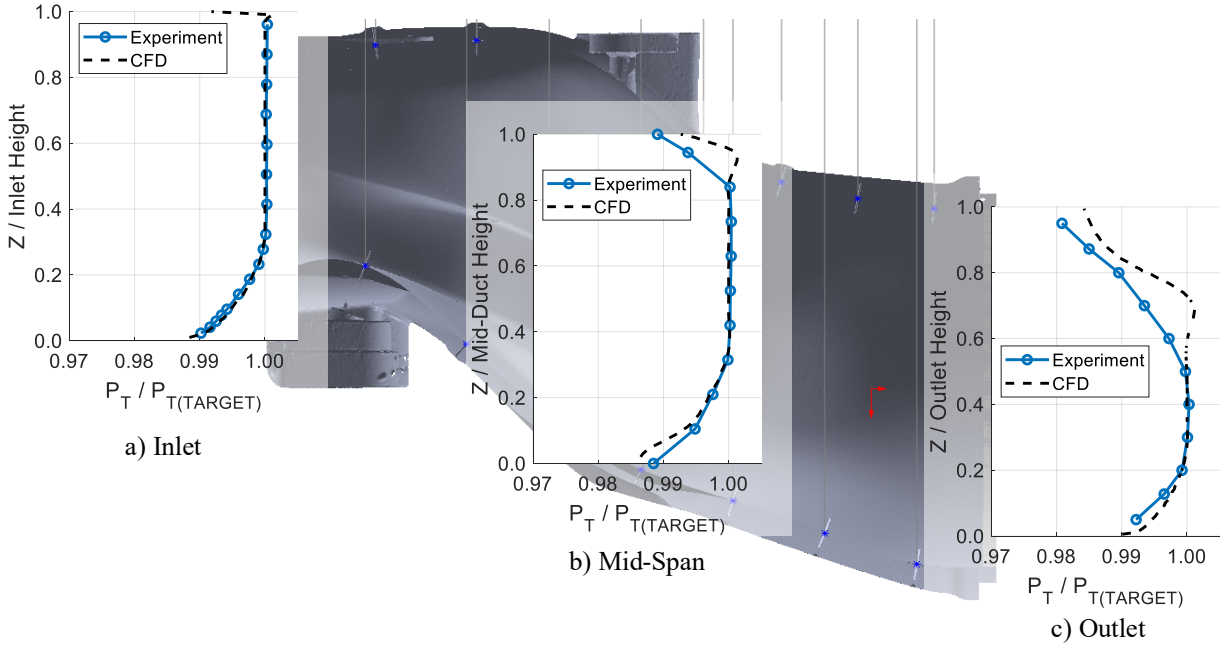

Fig. 10 Target Condition Centerline Total Pressure Profiles Within Duct

C. Outlet Profiles

A comparison of the CFD and experimental outlet total pressure profiles is provided in Fig. 11, and a comparison of the total pressure recovery, distortion and swirl for the CFD and experimental data at the target optimization conditions is provided in Table 2.

To ensure that no significant flow field features were missed due to the coarseness of the traverse grid at the outlet, a run was completed at the target condition with a more refined grid. The results do not show any significant differences within the measurement area of the regular grid. The results do show that some of the flow distortion closest to the wall was missed with the regular grid, which is why there is an increase in calculated distortion and swirl for the refined grid. For future test programs it would be beneficial to add an extra radial position for data closer to the outer wall, despite the extra sampling time required.

The experimental results confirm the ability of the optimization software to design an S-duct that minimizes distortion while maximizing total pressure recovery at the outlet. The experimental data show a somewhat higher distortion than predicted by CFD. There are also some minor asymmetries in the experimental profile that are likely due to non-uniformities in the inlet flow and manufacturing tolerances of the S-duct geometry. The calculated values for swirl match well between the refined experimental grid and the CFD, indicating again that an extra radial point closer to the added wall is needed for future work to better capture the entire flow field performance.

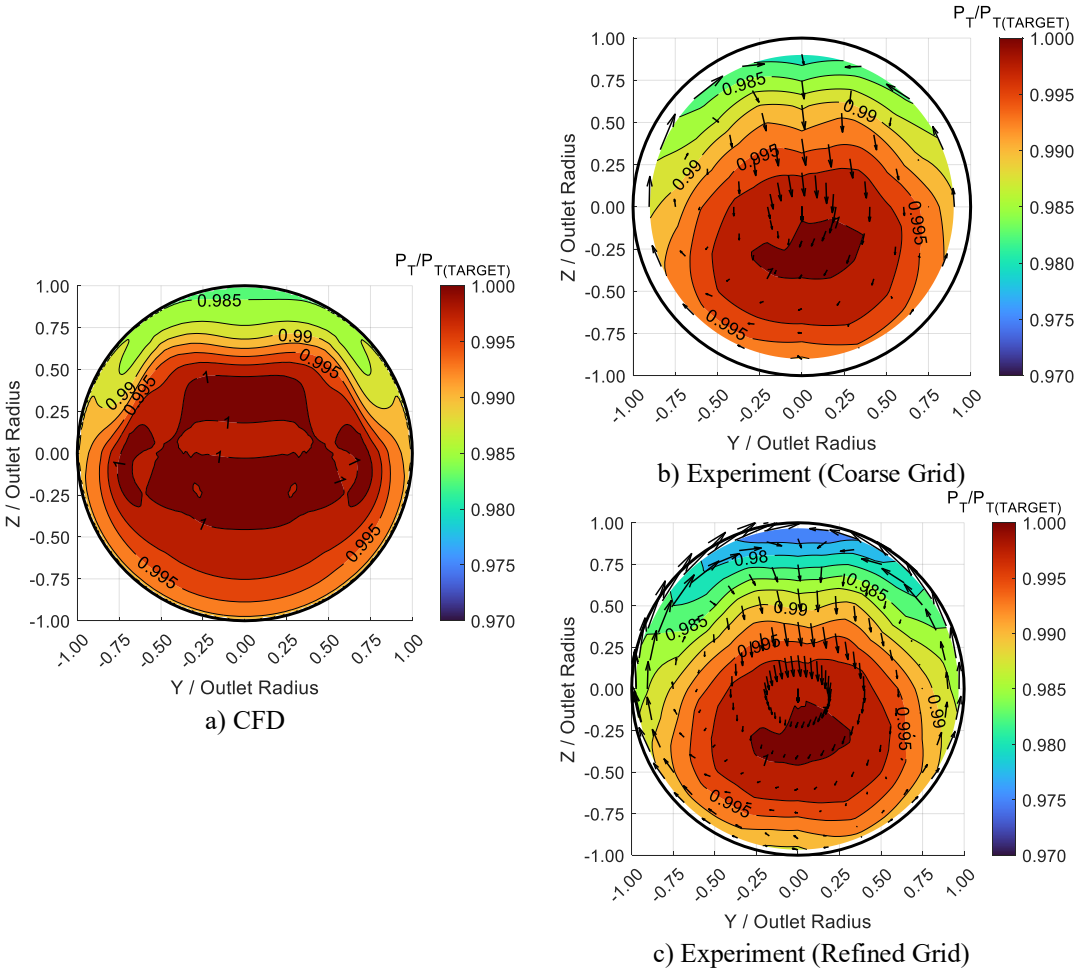

Fig. 11 Target Condition Outlet Total Pressure Profiles

Table 2 Target Condition S-Duct Performance

Mach	BLI Height (% Inlet)	Total Pressure Recovery	Distortion	Swirl (rad)
Optimized CFD	35%	0.9974	3.1 e-05	0.139
Experiment	34% (Regular Grid)	0.9945	5.7 e-05	0.097
	33% (Refined Grid)	0.9929	11.8 e-05	0.114

VI.Parametric Study of Off-Design Conditions

A secondary goal of the research program was to examine the sensitivity of the S-duct performance to off-design conditions. This was done by changing both the boundary layer thickness at the inlet and changing the mass flow rate (Mach number) through the test rig.

A. Inlet Profiles

The inlet uniformity Mach contours with varying boundary layer thicknesses are presented in Fig. 12 and the centerline total pressure and Mach number profiles are provided in Fig. 13, for a target Mach number of 0.16. There were no significant differences observed in the inlet profiles at Mach 0.19, which are not presented. As previously observed when completing the BLG calibrations, there is an increase in non-uniformity in the boundary layer thickness across the span of the inlet as the BLG mass flow rate increases.

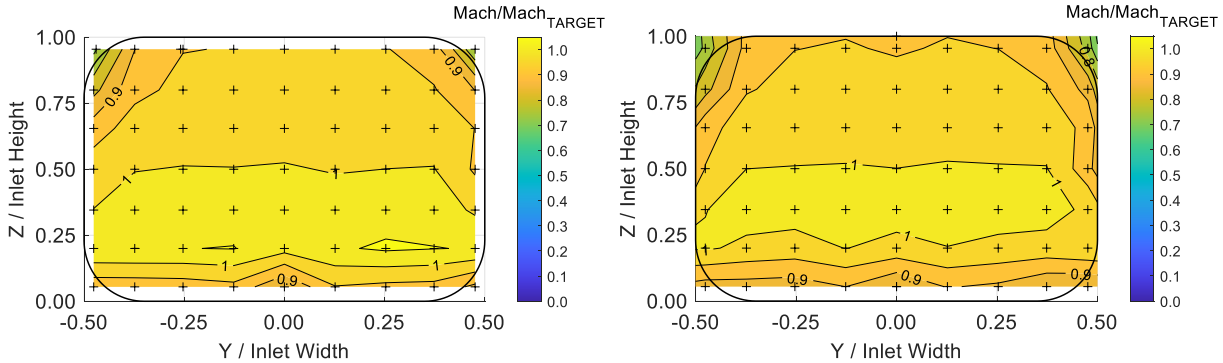

a) Boundary Layer Thickness = 20%

b) Boundary Layer Thickness = 34%

c) Boundary Layer Thickness = 50%

d) Boundary Layer Thickness = 69%

Fig. 12 Parametric Study Inlet Mach Contours (Mach 0.16)

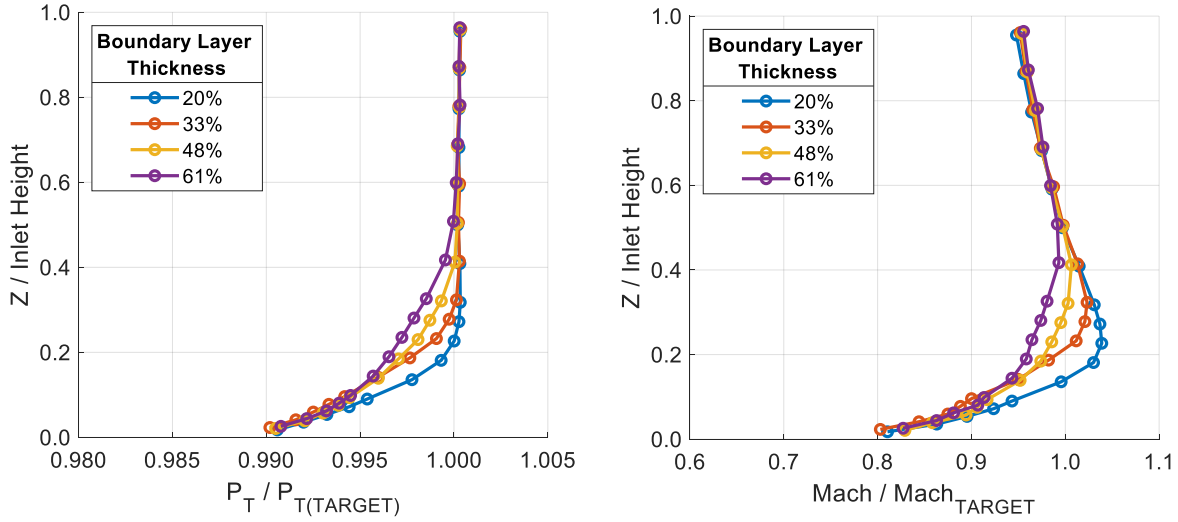

Fig. 13 Parametric Study Inlet Centerline Profiles (Mach 0.16)

B. Flow Within Duct

The flow profiles measured experimentally throughout the duct at different inlet Mach numbers and boundary layer thicknesses are presented in Fig. 14. The results show that the upper half of the flow (from 50 to 100% of the height) is insensitive to the incoming boundary layer thickness, with almost no difference in the profiles at a given inlet Mach number throughout the length of the duct. The lower half of the flow (from 0 to 50% of the height) maintains a boundary layer thickness proportional to the inlet boundary layer thickness at the mid-length of the duct, but starts to shrink as the ceiling boundary layer thickens and the two interact at the outlet of the duct. The inlet and mid-length pressure profiles for the two inlet Mach numbers are similar, although the profiles for Mach 0.19 show a slight decrease in total pressure closer to the walls compared to Mach 0.16. The largest differences are observed at the outlet, where the profile for Mach 0.19 suggests the flow near the ceiling may be close to or has already separated under the adverse pressure gradient along the ceiling, as indicated by the inflection point in the boundary layer curve near the ceiling.

Note that there are no results presented at the outlet for Mach 0.19 with 35% target boundary layer thickness due to an error in the data acquisition at that condition.

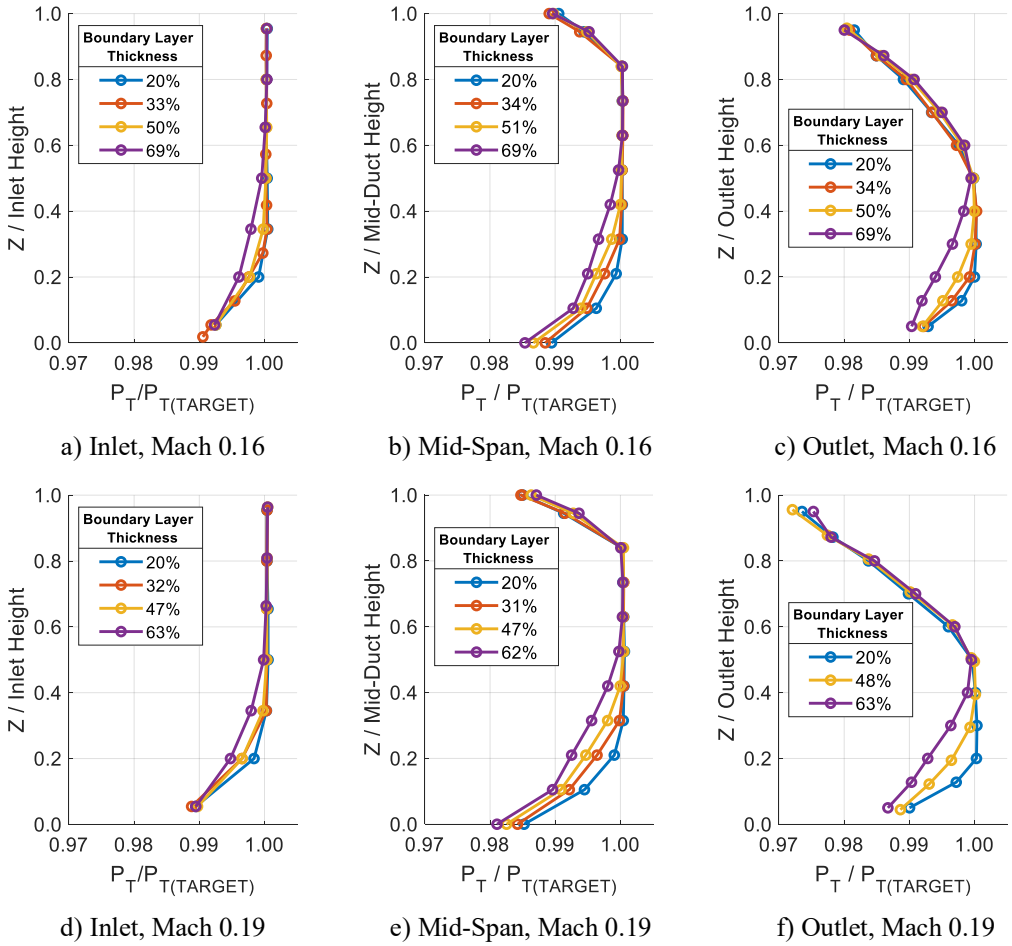

a) Inlet, Mach 0.16 b) Mid-Span, Mach 0.16 c) Outlet, Mach 0.16

d) Inlet, Mach 0.19 e) Mid-Span, Mach 0.19 f) Outlet, Mach 0.19

Fig. 14 Parametric Study Centerline Total Pressure Profiles Within Duct

C. Outlet Profiles

The experimental total pressure recovery, circumferential flow distortion, and swirl are examined at Mach 0.16 and Mach 0.19 as a function of the inlet boundary layer thickness in Fig. 15. Note again that there are no results presented for Mach 0.19 with 35% target boundary layer thickness due to an error in the data acquisition at that condition. Also note that only the trends from these results should be interpreted, not the absolute values, as additional measurements closer to the outer radius of the outlet are required to better capture all of the flow features near the walls of the duct, as previously discussed.

The results show that the total pressure recovery ratio is generally insensitive to boundary layer thickness, and the pressure recovery increases as the Mach number decreases. This is expected, as at a higher Mach number there are higher losses due to skin friction on the walls and potentially flow separation at the outlet.

The distortion at the outlet is a nominally linear function of the boundary layer thickness, with the distortion decreasing as the boundary layer thickness increases. As is observed in the profiles presented in Fig. 16 and Fig. 17, as the boundary layer thickness increases, the peak pressure of the outlet profile moves closer to the middle of the duct and reduces the circumferential distortion. Although the location of the peak pressure at the outlet doesn't appear to change with Mach number, the gradient as the pressure drops off towards the outside radius of the duct increases, which increases the calculated distortion at the higher Mach number. It is also worth noting that the non-uniformities at the inlet with the higher BLG flow rates do not appear to have a significant impact on the profiles at the outlet.

The swirl does not appear to be a function of Mach number, and decreases non-linearly as the boundary layer thickness at the inlet increases and the peak pressure at the outlet moves towards the center.

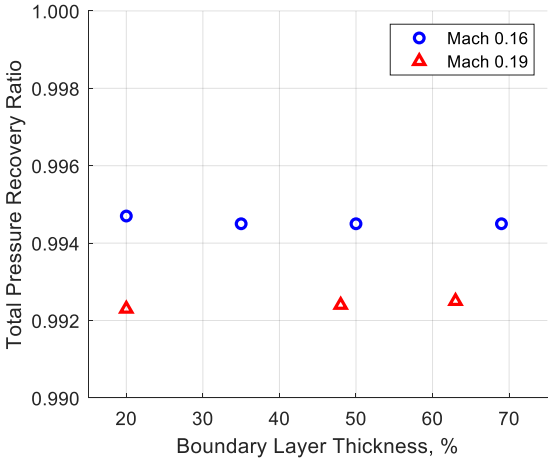

a) Total Pressure Recovery

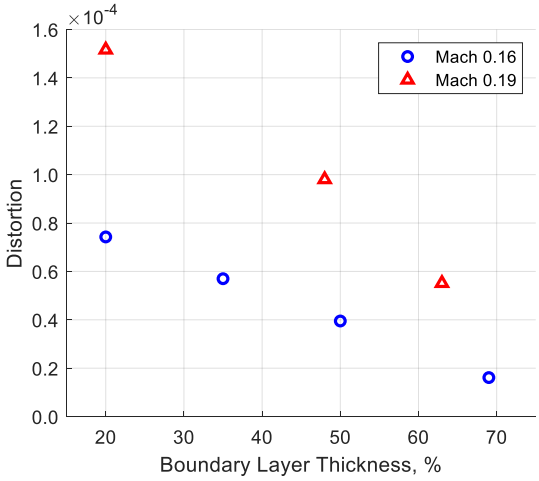

b) Distortion

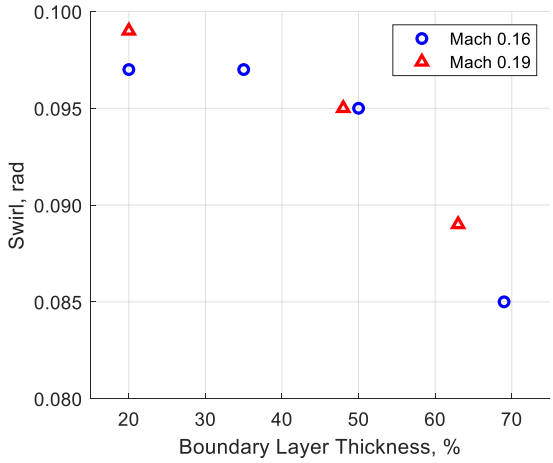

c) Swirl

Fig. 15 Parametric Study S-Duct Performance Summary

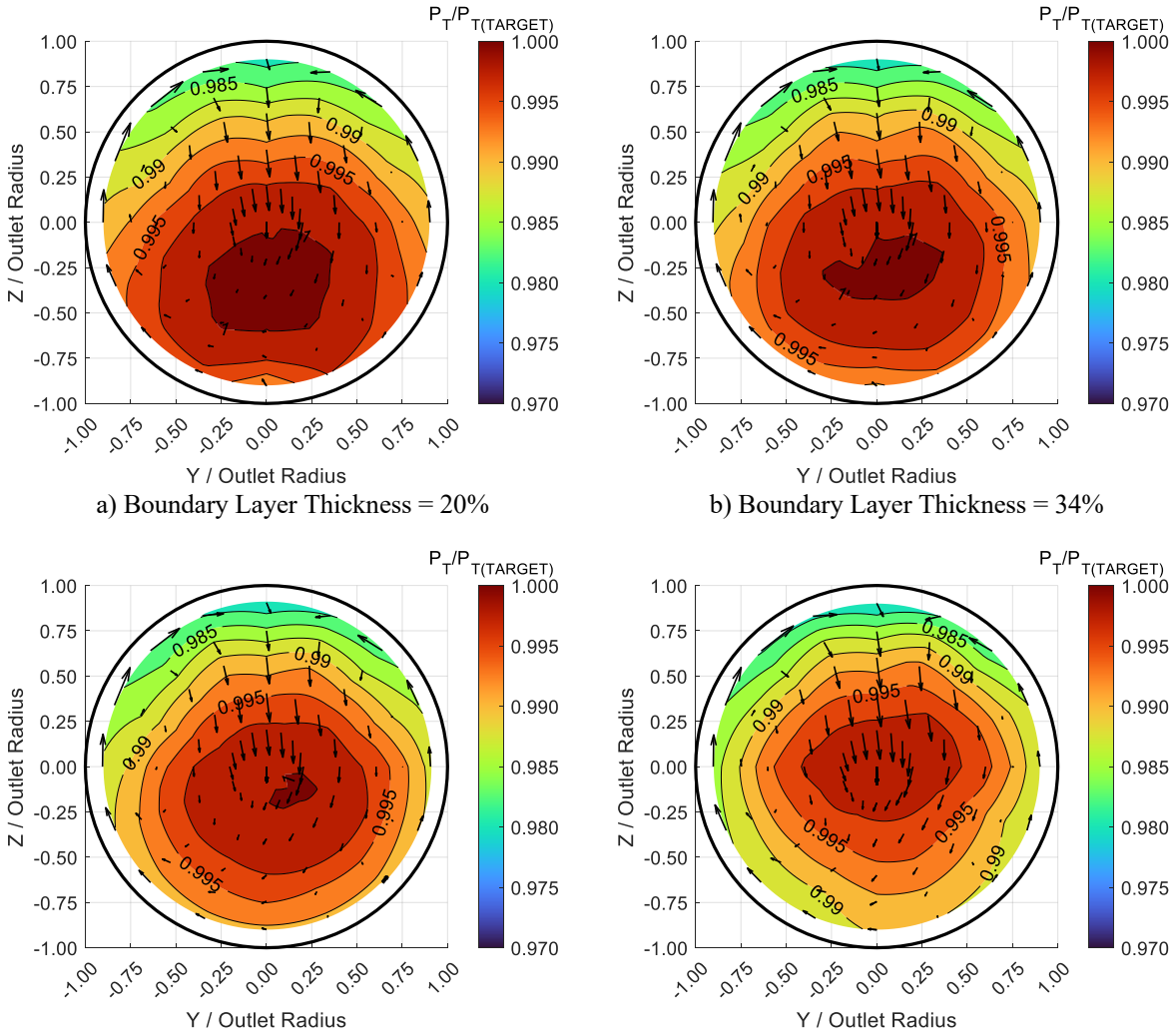

a) Boundary Layer Thickness = 20%

b) Boundary Layer Thickness = 34%

c) Boundary Layer Thickness = 50%

d) Boundary Layer Thickness = 69%

Fig. 16 Parametric Study Outlet Total Pressure Profiles (Mach 0.16)

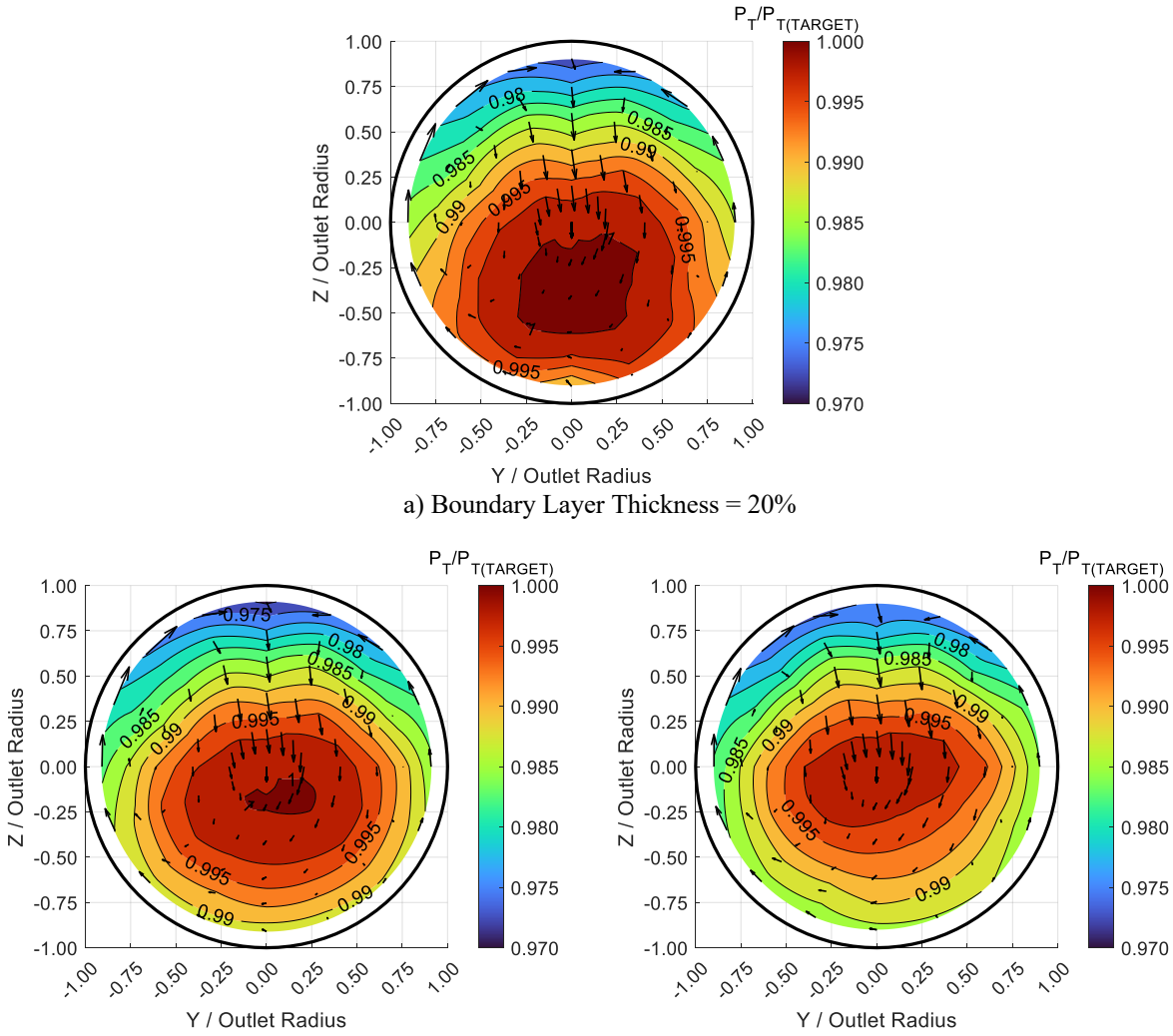

a) Boundary Layer Thickness = 20%

b) Boundary Layer Thickness = 48%

c) Boundary Layer Thickness = 63%

Fig. 17 Parametric Study Outlet Total Pressure Profiles (Mach 0.19)

VII. Conclusions and Recommendations

The experimental validation of the UTIAS S-duct optimization code was successfully completed in the NRC GTL's Test Cell 1 in the summer of 2023. The validation exercise included the design, construction and calibration of a boundary layer ingestion test rig that includes the ability to test at various Mach numbers up to 0.28 and simulated total pressures down to 38 kPa. The BLG calibrations showed that the boundary layer thickness could be controlled within the range of desired target conditions, although the uniformity could be improved at the higher BLG mass flow rates.

Despite some variation in the location of the peak pressure at the outlet, there is reasonably good agreement between the CFD and experimental data that confirms the ability of the UTIAS optimization code to minimize circumferential distortion and maximize pressure recovery through geometric design. Based on these results, the second phase will continue in 2024 that will include the incorporation of an electric motor and fan into the simulations and experimental set-up.

The parametric study on the effects of boundary layer thickness and Mach number showed that the distortion at the fan location is significantly impacted by the thickness of the boundary layer at the inlet. This suggests that the S-duct geometry optimization for a BLI-aircraft should include a parameter that evaluates the sensitivity of the geometry to the incoming boundary layer thickness, rather than just targeting a single condition for optimization, as the thickness can vary significantly depending on the angle of attack of the aircraft. The total pressure recovery was not as sensitive to boundary layer thickness but was sensitive to Mach number, with the experimental data indicating a potential for

separation near the upper surface of the outlet that should be considered as a sensitive area in future designs. The swirl value was insensitive to Mach number and showed good agreement between the CFD and experimental data.

Acknowledgments

The authors would like to acknowledge the support of the NRC Low-Emissions Aviation Program and NRC Aerospace Research Center for funding this project. The authors would also like to acknowledge the support of the technical staff at the NRC Gas Turbine Laboratory in ensuring the project's success.

References

[1] Drela, M., "Power Balance in Aerodynamic Flows," *AIAA Journal*. Vol. 47, No. 7, 2009, pp. 1761-1771. doi: 10.2514/1.42409

[2] Uranga, A., Drela, M., Greitzer, E.M., Hall, D., Titchener, N.A., Lieu, M.K., Siu, N.M., Casses, C., Huang, A.C., Gatlin, G.M., and Hannon, J., "Boundary Layer Ingestion Benefit of the D8 Transport Aircraft," *AIAA Journal*, Vol. 55, No. 11, 2017, pp. 3693-3708. doi: 10.2514/1.J055755

[3] Hall, D.K., "Analysis of Civil Aircraft Propulsors with Boundary Layer Ingestion," Ph.D. Thesis, Massachusetts Institute of Technology, Cambridge, MA, USA, 2015

[4] Sato, S., "The Power Balance Method for Aerodynamic Performance Assessment," Ph.D. Thesis, Massachusetts Institute of Technology, Cambridge, MA, USA, 2012.

[5] Gladin, J., Sands, J., Kestner, B., and Mavris, D., "Effects of boundary layer ingesting (BLI) propulsion systems on engine cycle selection and HWB vehicle sizing," *50th AIAA Aerospace Sciences Meeting including the New Horizons Forum and Aerospace Exposition*, AIAA paper 2012-0837, Nashville, TN, USA, 9-12 January 2012. doi: 10.2514/6.2012-837

[6] Uranga, A., Drela, M., Greitzer, E.M., Hall, D.K., Titchener, N.A., Lieu, M.K., Siu, N.M., Casses, C., Huang, A.C., Gatlin, G.M., et al., "Boundary Layer Ingestion Benefit of the D8 Transport Aircraft," *AIAA Journal,* Vol. 55, No. 11, 2017, pp. 3693-3708. doi: 10.2514/1.J055755

[7] Koo, D., Zingg, D., Chishty, W., and abo el Ella, H., "Optimizing Intakes for Embedded Engines," *24th ISABE Conference,* ISABE-2019-24290, Canberra, Australia, September 2019.

[8] Sudasinghe, A., Rajakareyar, P., Matida, E., abo el Ella, H., and ElSayed, M.S.A., "Aerodynamic Shape Optimization of an Aircraft Propulsor Air Intake with Boundary Layer Ingestion," *Journal of Applied Mechanics,* Vol. 3, No. 3, 2022, pp. 1123-1144. doi: 10.3390/applmech3030064

[9] Rasimarzabadi, F., Neuteboom, M., Clark, C., and Martensson, H., "Aerodynamics Analysis of a High-Speed Test Rig for use in Engine Test Facilities," *32nd Congress of the International Council of the Aeronautical Sciences,* ICAS-2020-0016, Shanghai, China, September 2021.

[10] Rasimarzabadi, F., Clark, C., Neuteboom, M., Orchard, D., and Martensson, H., "An Altitude Capable Rig for Studying Engine Inlet Velocity Profile Effects," *25th ISABE Conference*, ISABE-2022-212, Ottawa, Canada, September 2022.

[11] Hicken, J.E. and Zingg, D.W., "Aerodynamic Optimization with Integrated Geometry Parameterization and Mesh Movement," *AIAA Journal*, Vol. 48, No. 2, 2010, pp. 401-413. doi: 10.2514/1.44033

[12] Gagnon, H. and Zingg, D., "Two-level Free-Form and Axial Deformation for Exploratory Aerodynamic Shape Optimization," *AIAA Journal*, Vol. 53, No. 7, 2015, pp. 2015–2026. doi: 10.2514/1.J053575

[13] Osusky, M. and Zingg, D. W., "A Parallel Newton-Krylov-Schur Flow Solver for the Reynolds-averaged Navier-Stokes Equations Discretized using Summation-by-Parts Operators," *AIAA Journal*, Vol. 51, No. 12, 2013, pp. 2833-2851. doi: 10.2514/1.J052487

[14] Osusky, L., Buckley, H.P., Reist, T.A.,and Zingg, D.W., "Drag Minimization based on the Navier-Stokes Equations Using a Newton-Krylov Approach," *AIAA Journal*, Vol. 53, No. 6, 2015, pp. 1555-1577. doi: 10.2514/1.J053457

[15] Reist, T. A., Koo, D., Zingg, D. W., Bochud, P., Castonguay, P., and Leblond, D., "Cross-Validation of High-Fidelity Aerodynamic Shape Optimization Methodologies for Aircraft Wing-Body Optimization," *AIAA Journal*, Vol. 58, No. 6, 2020, pp. 2581-2595. doi: 10.2514/1.J059091

[16] Chiang, C., Koo, D., and Zingg, D.W., "Aerodynamic Shape Optimization of an S-Duct Intake for a Boundary-Layer Ingesting Engine", *Journal of Aircraft*, Vol. 59, No. 3, 2022, pp. 725-741. doi: 10.2514/1.C036632

[17] Roberts, J., & Walker, G., "Artificial thickening of wind tunnel boundary layers via an array of cross-flow jets," *Experimental Thermal and Fluid Science*, Vol. 27, No. 5, 2003, pp. 583-588. doi:10.1016/S0894-1777(02)00272-8

[18] Sargison, J., Walker, G., Bond, V., & Chavalier, G. "Experimental Review of Devices to Artificially Thicken Wind Tunnel Boundary Layers," *15th Australasian Fluid Mechanics Conference*, Sydney, December 2004.
[19] Pratte, B., & Baines, W., "Profiles of the Round Turbulent Jet in a Cross Flow," *Journal of the Hydraulics Division*, Vol. 93, No. 6, 1967, pp. 53-64.
doi: 10.1061/JYCEAJ.0001735